VIBRATIONAL ANALYSIS OF PALYGORSKITE AND SEPIOLITE

DAVID A. MCKEOWN[1,*], JEFFREY E. POST[2] AND EDGAR S. ETZ[3]

[1] Vitreous State Laboratory, The Catholic University of America, 620 Michigan Ave., N.E. Washington D.C. 20064, USA
[2] Department of Mineral Sciences, Smithsonian Institution, Washington, D.C. 20560-0119, USA
[3] Surface and Microanalysis Science Division, National Institute of Standards and Technology, Gaithersburg, Maryland 20899-0001, USA

Abstract—Lattice dynamic calculations for the sepiolite and palygorskite structures using polarized Raman and FTIR spectra provide a fundamental basis for interpreting spectral features by assigning vibrational modes. The $Si-O$ stretch and $O-Si-O$ bond bending force constants determined for palygorskite are similar to equivalent values calculated previously for other phyllosilicates. The $Mg-O$ bond stretch values, on the other hand, are about half of those determined for the equivalent $Al-O$ and $Mg-O$ bond stretch environments in other phyllosilicates, suggesting that the bonding within the octahedral ribbons in palygorskite and sepiolite is weaker than that in the continuous octahedral sheets in micas. The weaker bonding allows more flexible octahedral environments in palygorskite and sepiolite, giving rise to higher probabilities for cation substitutions and vacancies relative to the micas. Above ~700 cm^{-1} in the IR and 750 cm^{-1} in the Raman spectra, the eigenmodes are dominated by atomic displacements within the silicate sheets. Below 700 cm^{-1} the eigenmodes become mixed with motions among the Mg octahedra and the silicate sheets; the eigenmodes assigned to the most prominent peaks in the Raman spectra (near 700 cm^{-1}) belong to this group. As mode frequencies decrease, the corresponding eigenmodes evolve from more localized Mg-O stretch, O-Mg-O bend and O-Si-O bend motions to longer-range motions such as silicate sheet deformations caused by silicate tetrahedra rotation and silicate sheet shearing around the Mg-octahedral sheets.

Key Words—FTIR, Palygorskite, Raman, Sepiolite.

INTRODUCTION

Sepiolite and palygorskite are hydrous Mg silicate clay minerals with fibrous-like morphologies that typically occur as fine-grained, poorly crystalline masses. They are found in a wide variety of geological environments and have been mined for centuries because of their many useful properties. Many of the more than 100 commercial uses today, *e.g.* in the pharmaceutical, fertilizer and pesticide industries (VanScoyoc *et al.*, 1979; Jones and Galán, 1988), utilize the large surface areas and microporous characteristics of the materials. In recent years, because of their structural morphologies, palygorskite and sepiolite have received considerable attention with regard to adsorption of organics, for use as supports for catalysts (Frost *et al.*, 1998), as molecular sieves (Ruiz-Hitzky, 2001), and as inorganic membranes for ultra-filtration (Wang *et al.*, 2001).

Palygorskite and sepiolite are layer structures built up of ribbons of 2:1 phyllosilicate modules that are themselves constructed of linked double and triple silicate chains, respectively, that sandwich (Mg,Al)-(O,OH) octahedral strips (Figure 1a,b). The ribbons are linked by inversion of the SiO$_4$ tetrahedra through $Si-O-Si$ bonds. The phases have continuous tetrahedral sheets, but with tetrahedral apices pointing in opposite directions in adjacent ribbons. Unlike other phyllosilicates, they lack continuous octahedral sheets. The

structures have large tunnels parallel to the phyllosilicate ribbons that are partially occupied by water molecules. The tunnels measure 3.7×10.6 Å and 3.7×6.4 Å in cross-section for sepiolite and palygorskite, respectively.

The sepiolite structure was first deduced by Brauner and Preisinger (1956) in space group *Pnan*. The monoclinic structure model proposed for palygorskite by Bradley (1940), space group *C2/m*, was later confirmed by Drits and Sokolova (1971). Several researchers have suggested that there is also an orthorhombic form of palygorskite (Preisinger, 1963; Christ *et al.*, 1969; Chisholm, 1992), and many samples appear to be mixtures of the two forms. Because of the fine-grained and typically poorly crystalline nature of these minerals, it has not been possible to study their crystal structures using single-crystal diffraction methods, and consequently many details of the structures are still not well known. In order to characterize better the structures and behaviors of these phases, researchers have used powder diffraction, electron microscopy, thermogravimetric and spectroscopic techniques. In particular, infrared (IR) spectroscopy has been used to study the nature of water in sepiolite and palygorskite structures as well as changes in their structures resulting from heating/dehydration (*e.g.* Hayashi, 1969; Mendelovici, 1973; Serna *et al.*, 1977; VanScoyoc *et al.*, 1979; Blanco *et al.*, 1988; Frost *et al.*, 1998) or compositional variations (Mendelovici and Portillo, 1976).

* E-mail address of corresponding author:
davidm@vsl.cua.edu

667
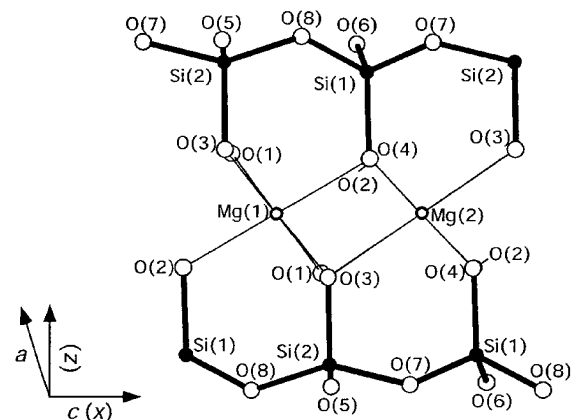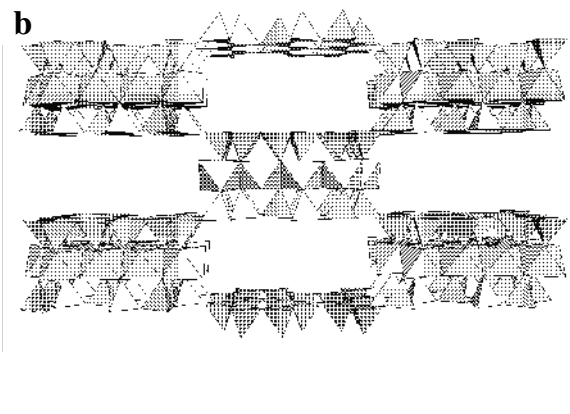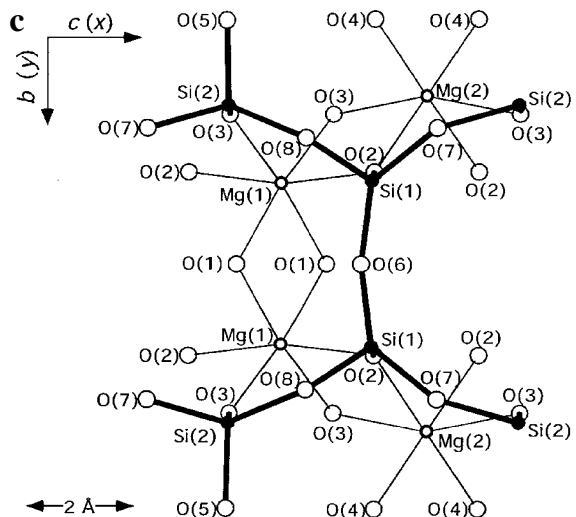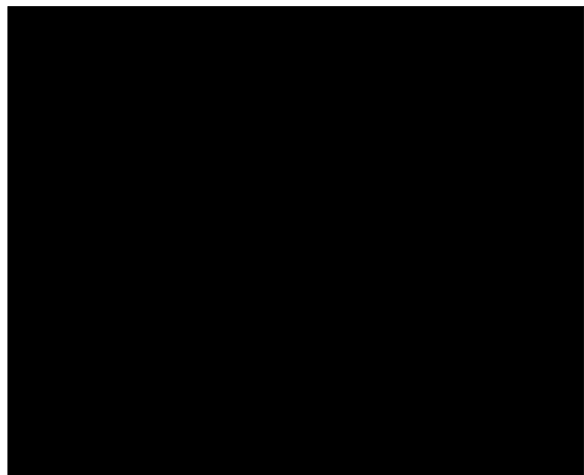
Figure 1. Polyhedral representations of the (a) palygorskite and (b) sepiolite crystal structures, looking along *c*. (c) The palygorskite crystal structure cluster used in the lattice dynamics calculations, showing crystallographic *a*, *b* and *c* axes in relation to the *x*, *y* and *z* axes used in the calculations.

In the present study, we describe the Raman and IR spectra of sepiolite and palygorskite. Lattice dynamic calculations of the zone-center optical phonons for these two structures were performed to provide a more fundamental basis for interpreting the spectra by assigning vibrational modes to the spectral features. The derived force constants and atomic displacements (eigenmodes) are compared with those reported for other phyllosilicates (McKeown *et al.*, 1999a,b).

EXPERIMENTAL

The sepiolite sample used for spectroscopic measurements (NMNH#92158-1) is from Durango, Mexico; and Rietveld refinements using powder X-ray data revealed that it is exceptionally well crystalline for sepiolite and free of impurity phases. Chemical analysis indicates that it has a composition that does not differ significantly from

the ideal formula: $Mg_2Si_3O_8 \cdot nH_2O$. Infrared spectra were collected for palygorskite samples from Alaska (NMNH#117101), $(Mg_{2.02},Al_{1.92},Fe_{0.08})$ $Si_{7.90}O_{21} \cdot nH_2O$; Yalu River, Korea (NMNH#R12180), $(Mg_{2.37},Al_{1.84},Fe_{0.07})Si_{7.87}O_{21} \cdot nH_2O$; and Glasgow, Virginia (NMNH#114540), $(Mg_{1.99},Al_{2.06},Fe_{0.02})$ $Si_{7.94}O_{21} \cdot nH_2O$; but as is explained below, suitable Raman spectra were obtained only from the Virginia sample. The palygorskite and sepiolite chemical formulae were determined by energy-dispersive analyses on a transmission electron microscope. Powder X-ray diffraction (XRD) patterns indicate that the first two palygorskite samples are the pure monoclinic polytype and that the Virginia sample consists mainly of the monoclinic phase with minor amounts of the orthorhombic phase. Powdered samples were ground to <10 μm diameter particles.

The IR spectra were collected using a Bio-Rad Excalibur FTS 3000 Fourier transform infrared spectro-
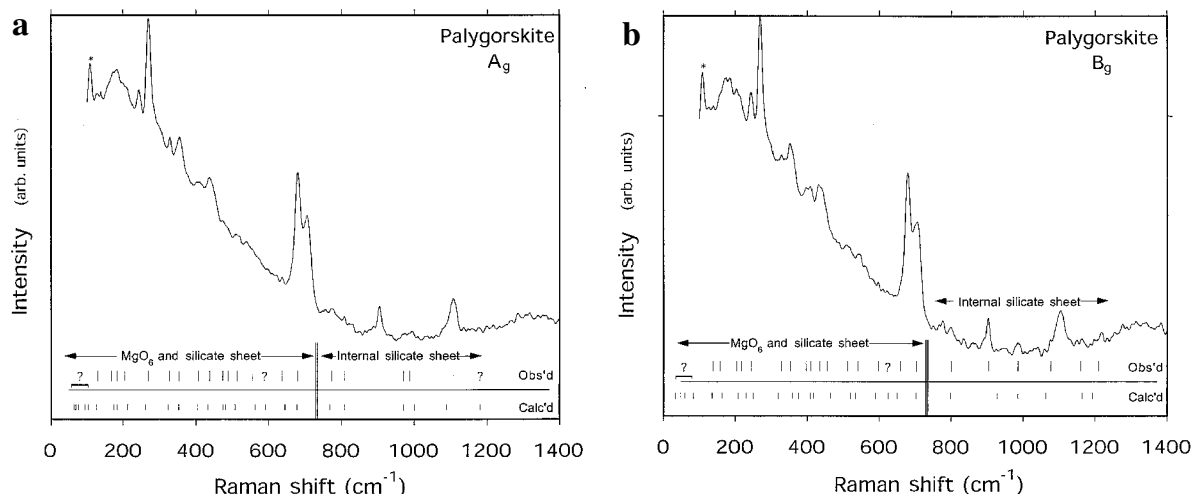
Figure 2. Raman spectra of palygorskite showing: (a) parallel polarized, A_g-dominated modes; and (b) cross-polarized, B_g-dominated modes. Observed mode frequencies to the spectra and the corresponding calculated mode frequencies as well as general vibrational assignments are indicated. ? indicates a calculated mode that cannot be unambiguously assigned to an observed mode in the spectrum. * indicates an artifact from the laser line filter cut-off.

meter. Transmission IR spectra were collected from pressed KBr pellets (~2.5 mg sample per 250 mg KBr) and from self-supporting thin films, prepared following the procedure of Ahlrichs *et al.* (1975). Each data set consisted of 64 co-added scans collected at 4 cm^{-1} resolution and corrected for background and instrument response. Far-IR spectra were collected for sepiolite from the self-supporting film and for palygorskite using a pressed polyethylene pellet on the same instrument using a 12.5 μm mylar beam splitter and DTGS far-IR detector. The IR spectra for all three palygorskite samples are essentially identical, and because the Virginia sample yielded the best Raman data, its IR spectrum was also used for the lattice dynamic calculations.

Polarized Raman spectra were obtained in back-scattering geometry using a Brüker FT-Raman instrument (Model RFS-100)*. The source was a Nd:YAG laser supplying 1064 nm wavelength excitation at 900 mW. Variable power densities were initially placed at the sample to make sure that no sample modification was incurred. The detection system consisted of a high-sensitivity germanium detector operated at liquid nitrogen temperatures. All spectra were recorded at 4 cm^{-1} resolution and were corrected for the instrument response function. Raman shift calibration ensured that band frequencies are accurate to within 1 cm^{-1}. In each scattering geometry, the FT-Raman spectrum was acquired through 600 co-added scans to optimize the

signal-to-noise ratio. Using near-IR excitation furnished spectra that greatly reduced laser-induced luminescence from the sample. Earlier measurements using 514.5 nm laser excitation on palygorskite and sepiolite specimens produced spectra containing broad-band luminescence that masked most, if not all, Raman spectral features. Even with near-IR excitation, it was necessary to look at several palygorskite samples, to find a sample that produced spectra with acceptably low luminescence. The Raman spectra presented for palygorskite from Virginia have the best Raman signal-to-noise characteristics of all data gathered for this study, but still have significant luminescence intensities at frequencies <650 cm^{-1} (Figure 2a,b).

The unground palygorskite and sepiolite samples used for the Raman experiments were leathery white sheets composed of bundles of fibers, randomly oriented in the sheet, where the sheet surface was perpendicular to the incident and scattered light propagation directions. The Raman spectra are shown in Figure 2. The procedure for determining the vibrational species contributing to each polarized Raman spectrum is outlined in Loudon (1964).

Normal coordinate analysis

Clusters of 52 and 192 atoms simulating the palygorskite (Figure 1c) and sepiolite structures, respectively, were used for the lattice dynamics calculations at zero wavevector. The atom coordinates were determined by Rietveld refinements using synchrotron powder XRD data for the sepiolite and Alaskan palygorskite (unpublished results). The clusters for each phase contained simplified octahedral environments that were occupied solely by Mg. The structural models for palygorskite and sepiolite excluded the water molecules in the tunnels.

Table 1. Irreducible representations for the palygorskite structure, excluding zeolitic water.

Atom types	Site symmetry	A_g (R)	B_g (R)	A_u (IR)	B_u (IR)
Mg(1), Mg(2)	2	1	2	1	2
O(1), O(6)	m	2	1	1	2
O(5)	i	0	0	3	3
Si(1), Si(2), O(2), O(3), O(4), O(7), O(8)	1	3	3	3	3
N_{total}		27	27	28	32

Note: Species followed by (R) and (IR) are Raman active and IR active, respectively. A_u and B_u species include 1 and 2 acoustic modes, respectively.

For sepiolite, H atoms in all hydroxides and water molecules bonded to Mg were taken into account by having atoms with masses for OH and H_2O bonded to Mg in the octahedral environments. The potential energy model used to describe the bonding for both structures is based on a valence force potential consisting of bond-stretching and bond-bending interactions. Initially, lattice dynamics calculations were performed on the palygorskite structure, following the procedure reported by Kim *et al.* (1993). Due to the more complicated crystal structure, the calculation for sepiolite used a different lattice dynamics calculations package (Dowty, 1987). To determine whether the results from both program packages were similar, the calculation for palygorskite was repeated using Dowty's procedure, with the program using the same atomic cluster and force constant values as those determined earlier. The resulting calculated frequencies and eigenmodes are nearly identical to those from the earlier calculation.

A total of 114 fundamental optical modes are predicted for the palygorskite structure by factor group analysis (FGA) using the methods of Fateley *et al.* (1972) and Dowty (1987), where 54 modes are Raman-active and 60 are IR active (Table 1). Many fundamental mode frequencies could be determined from the Raman and IR spectra, and they provided targets for the calculations. The calculations, in turn, provided guidelines for making additional fundamental mode assignments, especially to weaker spectral features. Variations between the A_g and B_g spectra are subtle (Figure 2). The most noticeable differences are slight intensity and peak-shape variations for some of the spectral features. Variations between the IR spectra of self-supporting films (oriented) and KBr pellet (random) samples for palygorskite are more noticeable (Figure 3), and some vibrational species assignments could be clearly made. There is no evidence from experiment or theory of combination or overtone modes in the data.

The calculations for the palygorskite structure used a total of 180 interactions described by eight force constant values (Table 2) that adequately depict the bonding environments in the structure, so that all fundamental optical modes were calculated to have non-zero frequencies. Initial lattice dynamics calculations were performed for palygorskite using force constant values for Si-O and Mg-O stretching and O-Si-O, Mg-O-Si and O-Mg-O bending similar to those determined for equivalent environments in the muscovite and phlogopite structures (McKeown *et al.*, 1999a,b). These initial values provided a good starting point for the calculations, as the program converged to a best fit of the theoretical Raman- and IR-active mode frequencies to the observed mode frequencies determined from the spectra. The eight force constants were adjusted to give the best fit between calculated and observed frequencies in the two Raman and two IR spectra (Figures 2 and 3). The fitting was accomplished by minimizing the root-mean-square (rms) deviation between the calculation and measurement (Kim *et al.*, 1993), where the rms deviation converged to 10.1 cm^{-1}. The calculated frequency and associated eigenmode for each Raman-active fundamental A_g or B_g mode for

Table 2. Force constant values calculated for palygorskite, muscovite and phlogopite.

| Interaction	Palygorskite	Phlogopite*	Muscovite*
Si−O(b)	4.85×10^5 dyne/cm	4.05×10^5 dyne/cm	4.56×10^5 dyne/cm
Si−O(nb)	4.82	4.55	4.11
Mg(1)−O	0.94	*M*(1)−O: 2.50	
Mg(2)−O	1.37	*M*(2)−O: 2.11	*M*(2)−O: 2.44
O(nb)−Si−O(b)	1.20×10^{-11} erg	2.08×10^{-11} erg	0.63×10^{-11} erg
O(b)−Si−O(b)	1.10	0.21	1.03
Mg−O−Si	0.22	0.11	0.38
O−Mg−O	0.08	−	−

* McKeown *et al.* (1999a,b)
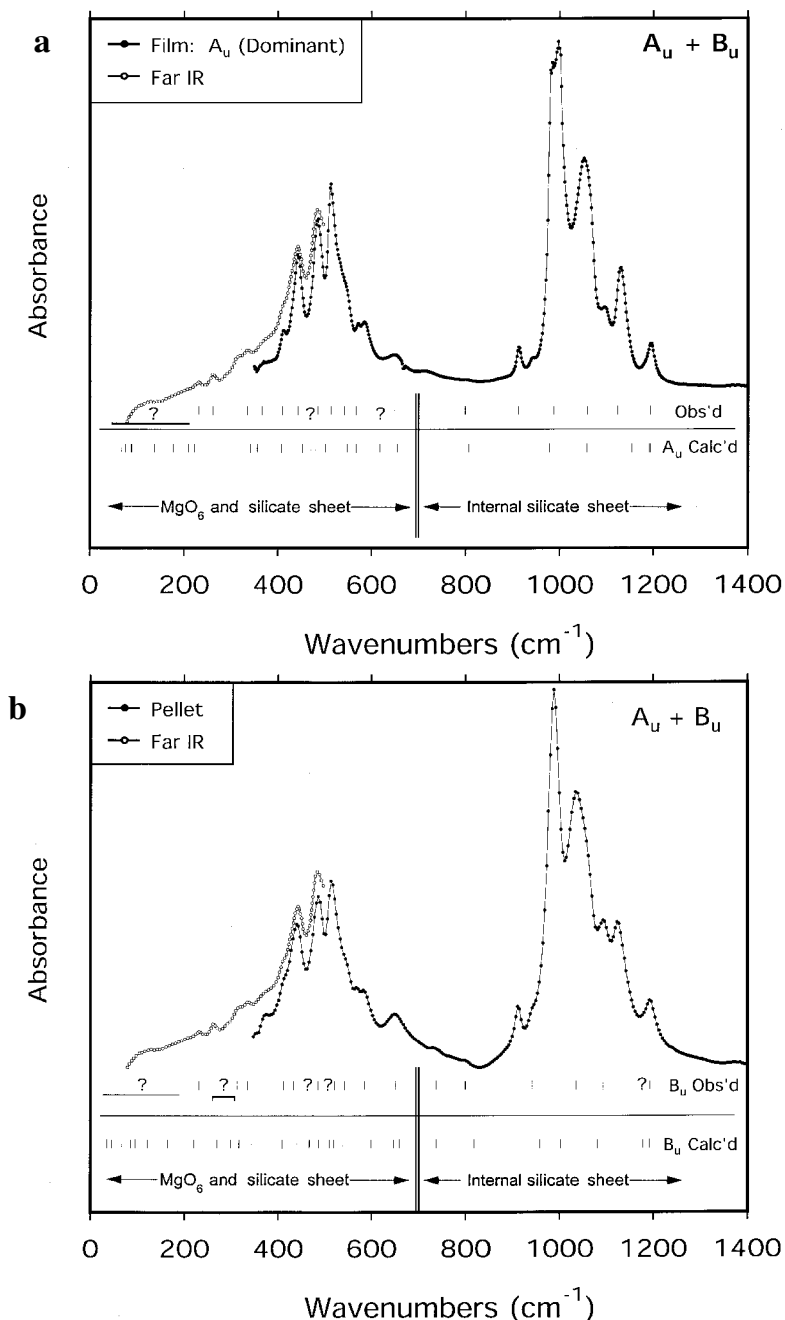
Figure 3. IR spectra of palygorskite: (a) A_u-dominated modes for the film sample; and (b) $A_u + B_u$ modes from the more randomly oriented crystals within the pellet sample. Conventions in Figure 2 apply.

palygorskite is listed in Tables 3 and 4, respectively, and plotted in Figure 2. Several representative Raman-active eigenmodes are shown in Figure 4. Calculated frequencies and mode assignments for the IR-active A_u and B_u species are listed in Tables 5 and 6, respectively, and plotted in Figure 3.

Calculations for the sepiolite structure and the resulting vibrational assignments to the observed Raman and IR fundamental modes required a different strategy than was used for palygorskite. For sepiolite,

FGA predicts 348 modes in eight vibrational species: 174 modes for the Raman-active A_g, B_{1g}, B_{2g} and B_{3g} species and 133 modes for the IR-active B_{1u}, B_{2u} and B_{3u} species (Table 7a). The large number of predicted optically active fundamental modes make it impossible to provide unambiguous vibrational assignments to all spectral features in the Raman and IR spectra for sepiolite (Figures 5 and 6), especially considering the relatively few resolved features that could be assigned to fundamental modes in the observed spectra.

Table 3. Observed and calculated frequencies for palygorskite, and assignments for the Raman-active A_g fundamental modes.

Experiment (cm^{-1})	Calculated (cm^{-1})	Assignment
–	63	Mg(2) octahedra $\pm y$; O(6)$\pm z$
–	68	MgO$_6$ deformation; O(1,4)$\pm xz$: in phase
–	76	MgO$_6$ deformation; O(1,4)$\pm xz$: out of phase
–	94	O(4)−Mg(2)−O(4) bend; O(1)$\pm xz$: out of phase
–	102	O(4)−Mg(2)−O(4) bend; O(1)$\pm xz$: in phase
130	126	Silicate tetrahedral ring deformation: O(7,8)$\pm z$; O(6)$\pm xz$; Si(1)−O(2)$\pm z$; Si(2)−O(3)$\pm z$
167	174	O(1)−Mg(1)−O(1) bend; O(6)$\pm xz$; Si(1) $+xz$
183	184	Mg(1)−O(1)−Mg(1) bend: Mg(1)$\pm y$; O(6)$\pm x$
205	212	Silicate sheet deformation: SiO$_4$ rotation $\parallel y$
268	262	Mg(2) octahedral deformation, Mg(2)$\pm y$ Si(1)−O(2)$\pm z$; O(6)$\pm zx$
327	323	MgO$_6$ octahedral breathing (Mg stationary); O(7)$+z$; O(8)$-z$
354	352	Si(2)−O(3)$\pm z$; O(1) $\pm xz$
406	405	Si(2)−O(3)$+z$; O(7)−Si(1)−O(8) bend
437	433	Mg(1)$\pm y$, MgO$_6$ octahedral rotation; O(6)$\pm xz$
473	474	Mg(1)$\pm y$; O(6)$\pm x$; O(1)$\pm xz$; O(6)−Si(1)−O(7) bend
488	480	O(2)−Si(1)−O(6) bend; O(7)$\pm y$
512	507	Mg(2) octahedral deformation, O(6)$\pm z$
556	562	O(3)−Mg(1)−O(3) bend
–	591	O(2)−Mg(2)−O(2) bend: Mg(2)$\pm y$; O(2,3)−Si(1,2)−O(7) bend
638	645	O(2)−Mg(2)−O(2) bend: Mg(2)$\pm y$; Si(2)$\pm y$; O(3)−Si(2)−O(8) bend
680	678	O(2)−Mg(2)−O(2) bend: Mg(2)$\pm y$; Si(2)$\pm y$; O(2)−Si(1)−O(6) bend
774	768	Si(1)−O(6)−Si(1) bend: Si(1)$+y$, Si(2)$-y$
809	809	Si(1)−O(7,8)−Si(2) bend: Si(1)$-x$, Si(2)$+x$
971	971	Si−O(nb) stretch: Si(1,2)−O(2,3)
988	1000	Si−O(nb) stretch: Si(1,2)−O(2,3)
1109	1090	O(8)−Si−(1)−O(7) bend
–	1182	Si−O(b) stretch: Si(1,2)−O(8,7)

The sepiolite samples can be pulled apart into leathery, sheet-like pieces, where the sheets contain quasi-randomly oriented bundles of fibers within the plane of the sheet. Ideally, it should be possible to collect parallel- and cross-polarized Raman spectra for sepiolite where the A_g modes (parallel-polarization) can be separated from the B_{1g}, B_{2g} and B_{3g} modes (cross-polarization). In reality, however, the differences between the two Raman spectra gathered for sepiolite are subtle (Figure 5), making it more difficult to assign unambiguously a vibrational species to each feature in the spectra. This ambiguity is due in part to the relatively weak intensities of most Raman features, especially above 400 cm^{-1}, with respect to the Fourier transform artifacts in the spectra. The scant polarization differences are also probably due to A_g modes that are within similar frequency ranges with respect to the B-species modes, where Raman intensities of the A_g modes are not much different than the sum of Raman intensities for all B-species modes. These small polarization differences are also observed for the polarized Raman spectra of the phyllosilicates muscovite and phlogopite (McKeown *et al.*, 1999a,b), especially for modes at frequencies above

300 cm^{-1}. The situation is similar for the sepiolite IR spectra (Figure 6).

In order to gain at least some insight into the vibrational assignments to the Raman and IR spectral features for sepiolite, an approximation was made with the model used by the lattice dynamics calculations. The crystal structures for palygorskite and sepiolite have similar Si and Mg coordination environments; the major differences between these two structures are the wider silicate and Mg octahedral ribbons for sepiolite with respect to palygorskite (Figures 1a and 1b). Because the lattice dynamics calculations are mostly influenced by localized bonding environments within a crystal structure, we assumed that the force constants describing the bonding in palygorskite are a good description of the localized bonding environments in sepiolite. Therefore, we assigned the final force constant values from the palygorskite calculation (Table 2) to comparable bond stretching and bond bending environments in sepiolite (Table 7b). The resulting calculation for the sepiolite cluster included a total of 640 interactions, described by eight force constants. The ultimate check for this model is the goodness of fit between the calculated frequencies and

Table 4. Observed and calculated frequencies for palygorskite, and assignments for the Raman-active B_g fundamental modes.

Experiment (cm^{-1})	Calculated (cm^{-1})	Assignment
–	32	Shear within each sheet $\pm x$; MgO$_6$ moving with shear: Mg(2)$\pm x$
–	46	O(4)$-$Mg(2)$-$O(4) rotation $\parallel x$
–	60	O(4)$-$Mg(2)$-$O(4) wagging; sheet rotation $\parallel x$
–	83	O(4)$-$Mg(2)$-$O(4) wagging; O(4,7)$\pm xz$; Si(1,2)$-$O(2,3)$\pm z$; sheet rotation $\parallel x$
139	136	Sheet shear around Mg sites: top sheet $+y$, bottom sheet $-y$; Mg(2)$\pm z$; O(2)$-$Mg(2)$-$O(4) bend
157	163	MgO$_6$ def.: Mg(1)$\pm xz$; Mg(2)$\pm z$; O(7,8)$\pm z$
205	208	Mg(1)$\pm xz$; O(1)$\pm y$
216	230	MgO$_6$ & sheet deformation: Mg(1,2)$\pm xz$; O(1)$\pm y$; Si(1)$-$O(6)$\pm y$
243	249	MgO$_6$ deformation: O(nb)$\pm xy$; Mg(1,2)$\pm xz$; O(7)$\pm y$
327	319	sheet rotation $\parallel x$; Si(1)$-$O(2) $+z$; Si(2)$-$O(3) $-z$
353	357	Si(2)$-$O(3)$\pm z$; Mg(1)$\pm x$; O(1)$\pm y$; O(7)$\pm z$
397	375	sheet deformation: Si(1)$\pm x$; O(7)$+y$; O(8)$-y$
410	409	O(2)$-$Mg(1)$-$O(2) rotation $\parallel x$; Mg(1)$\pm xz$; O(8)$\pm z$
435	418	Mg(1)$-$O(1) stretch; Mg(1,2)$+xz$; O(1)$\pm y$; O(8)$+z$; O(7) $-z$
456	464	Mg(1,2)$\pm xz$, O(8)$\pm z$; O(1)$\pm y$
512	520	Mg(1,2)$\pm xz$, Mg(1)$-$O(2) stretch; Si(2)$-$O(3)$\pm z$
540	534	MgO(1,2)$-$O(2,4) stretch; Si(1)$-$O(6)$\pm y$
597	589	MgO$_6$ deformation: Mg(1,2)$\pm zx$, Mg(1)$-$O(2) stretch; O(7)$\pm z$; O(2)$-$Mg(2)$-$O(3) bend
–	625	Mg(2)$-$O(2) stretch; O(7)$-$Si(2)$-$O(8) bend
658	649	Mg(2)$-$O(3) stretch, Mg(2)$\pm x$, O(8)$\pm zx$
704	702	Si(2)$\pm y$, O(6)$\pm y$ alternating per sheet
800	799	Silicate tetrahedral sheet shear: Si(1)$+x$; Si(2) $-x$; O(7,8)$\pm xz$
904	927	Si$-$O(nb) stretch: Si(1)$-$O(2); Si(1) tetrahedral base breathing
986	986	Si$-$O(nb) stretch: Si(2)$-$O(3)
1077	1063	Si$-$O(nb) stretch: Si(1)$-$O(2); Si(1) tetrahedral base breathing
1160	1164	Si$-$O(b) stretch: Si(1,2)$-$O(6,8)
1211	1193	Si$-$O(nb) stretch: Si(1,2)$-$O(6,7)

the observed Raman and IR spectral features; this turns out to be reasonably good as seen in Figures 5 and 6.

RESULTS AND DISCUSSION

Force constant values

One objective of this study was to determine whether the force constant values calculated previously for the phyllosilicates muscovite and phlogopite (McKeown *et al.*, 1999a,b) are comparable to those determined for palygorskite and sepiolite. The force constant values determined here (Table 2) indicate that this is the case for bonding within the silicate sheets in palygorskite and sepiolite. The Si-nonbridging-oxygen [Si-O(nb): or Si-O(1,2,3 or 4), see Figure 1c] bond-stretch value for palygorskite is within the range of equivalent force constant values calculated for the other phyllosilicates (Table 2); the Si-bridging-oxygen [Si-O(b): or Si-O(5,6,7 or 8), see Fig.1c] force constant for palygorskite is within 10% of that determined for muscovite. The O$-$Si$-$O bond bending force constants determined for palygorskite are also well within the broad range of equivalent values calculated for the other phyllosilicates (Table 2). The largest discrepancies in force constants between palygorskite-sepiolite calculations and the calculation results for the other phyllosilicates are observed for the bonding

within the octahedral sheets. The Mg$-$O bond stretch values for palygorskite are about half of those determined for the equivalent Al$-$O and Mg$-$O bond stretch environments in the octahedral sheets in muscovite and phlogopite, respectively. These force constant differences suggest that the bonding within the octahedral ribbons in palygorskite and sepiolite is weaker than that in the continuous octahedral sheets in muscovite or phlogopite. The weaker bonding leads to more flexible octahedral environments in palygorskite and sepiolite, giving rise to higher probabilities for cation substitutions and vacancies relative to the micas (*e.g.* as observed by Galán and Carretero, 1999).

Frequencies of calculated modes vs. observed Raman- and IR-active modes

Palygorskite. The calculations fit theoretical fundamental mode frequencies to the frequencies of features observed in the A_g and B_g Raman spectra so that eigenmodes can be unambiguously assigned to most peaks in the data (Figure 2). The peaks that clearly stand out from the Fourier transform ripples in the spectra, A_g modes at 167, 183, 205, 268, 327, 354, 437, 680, 971, 988 and 1109 cm^{-1} and B_g modes at 205, 216, 243, 353, 397, 410, 704, 800, 904 and 986 cm^{-1}, can be readily fit and described by the calculations. The selection of

Table 5. Observed and calculated frequencies for palygorskite, and assignments for the IR-active A_u fundamental modes.

Experiment (cm^{-1})	Calculated (cm^{-1})	Assignment
–	0	Acoustic $\pm y$
–	67	O(4)$\pm xz$, O(4)$-$Mg(2)$-$O(4) bend
–	76	MgO$_6$ deformation: O(4)$-$Mg(2)$-$O(4) bend, Mg(1)$-$O(6)$\pm x$, O(4,5)$\pm z$
–	88	O(4)$-$Mg(2)$-$O(4) bend
–	90	O(3,4)$-$Mg(1,2)$-$O(3,4) bend; sheet def.: O(5)$\pm z$, Si(1,2)$-$O(8,7)$\pm x$
–	138	Silicate sheet shear across $xz-$mirror plane
–	177	MgO$_6$ deformation
–	210	Mg(1)$-$O(1)$\pm y$; O(5)$\pm z$
231	222	Si(2) tetrahedral rotation $\parallel z$
262	257	MgO def.; tetrahedral sheet rotation $\parallel x$: top sheet clock-wise, bottom sheet counter-clockwise
335	342	Si(1)$-$O(2)$\pm z$; O(2,3)$-$Mg(1)$-$O(2,3) bend
366	356	Silicate sheet deformation: Si(2)$-$O(3)$+z$, Si(2)$-$O(5)$+x$, MgO$_6$ breathing
411	408	O(2)$-$Mg(1,2)$-$O(2) bend: O(2)$\pm xy$, O(1,6)$\pm y$
443	453	MgO$_6$ deformation, Mg(1)$\pm y$, O(1)$\pm y$, O(3)$-$Mg(1)$-$O(3) bend, O(5)$\pm z$
–	470	MgO$_6$ deformation, Mg(1)$\pm y$, O(1)$\pm y$, O(3)$-$Mg(1)$-$O(3) bend, O(5)$-xz$
486	481	MgO$_6$ deformation, Mg(1)$\pm y$, O(1)$\pm y$, O(3)$-$Mg(1)$-$O(3) bend, O(5)$+xz$
513	501	O$_6$ deformation: Mg(2,4)$\pm xz$, Mg(2)$-$O(2,4) bend; Si(2)$-$O(5,7)$\pm xz$
542	548	Silicate tetrahedra base deformation along y
567	567	MgO$_6$ deformation, O(8)$\pm z$
–	617	O(2,3)$-$Mg(2)$-$O(2,3) bend, Mg(2)$\pm y$, O(7)$\pm z$
650	655	O(2,3)$-$Mg(2)$-$O(2,3) breathing, Mg(2)$\pm y$, O(7,8)$\pm z$
799	807	Silicate sheet (ring) deformation: Si(1,2)$\pm x$
912	902	Silicate tetrahedra breathing
988	978	Si$-$O(nb) stretch: Si(1,2)$-$O(1,3)
1059	1058	Si(1,2)$-$O(2,3) stretch; tetrahedral base breathing
1124	1154	Si(1)$-$O(6) stretch, O(5)$-$Si(2)$-$O(8) breathing
1193	1191	Si$-$O(b) stretch: Si(2)$-$O(5)
1193	1193	Si$-$O(b) stretch: Si(1)$-$O(6), Si(1)$-$O(7), Si(2)$-$O(7)

weaker spectral features as fundamental modes was more subjective with respect to differentiating between fundamental modes and Fourier transform artifacts. The calculated mode frequencies provided some guidance in selecting many of the relatively weak fundamental mode spectral features and their observed frequencies. In some cases, weak observed fundamental modes were selected by comparing several spectra having the same scattering conditions, to see which features remained constant and which features varied as different Fourier transform conditions were used for each spectrum.

Observed IR fundamental mode frequencies were also used in the fitting process, where six A_u and six B_u mode frequencies above 600 cm^{-1} could be fit as target frequencies and described by the calculations. Some of the selection rules between the A_u and B_u species peaks are clearly seen in the higher frequency modes. The B_u modes at 941, 1034 and 1092 cm^{-1} are more prominent in the pressed-pellet spectrum than in the film spectrum where A_u modes are dominant. The theory predicts more modes below 600 cm^{-1} than the number of peaks that

are clearly seen in an envelope of overlapping features between 200 and 600 cm^{-1}. In this case, observed frequencies could not be unambiguously assigned to seven calculated modes; these calculated mode frequencies were allowed to vary without a target frequency to fit (Figure 3).

Sepiolite. The calculations for the sepiolite structure determined many more fundamental mode frequencies than resolved fundamental mode features in the Raman and IR spectra; therefore, no observed fundamental mode frequencies were used and no fitting was done. Due to the subtle differences between the parallel-polarized (A_{1g}-dominated) and the cross-polarized (B_{1g}-, B_{2g}- and B_{3g}-dominated) Raman spectra, the vibrational species could be assigned for only a few peaks (Figure 5); this was done by assigning the species of calculated modes that best match frequencies with a particular observed mode.

There are noticeable differences between the IR spectra (Figure 6) of the pressed-pellet (randomly

Table 6. Observed and calculated frequencies for palygorskite, and assignments for the IR-active B_u fundamental modes.

Experiment (cm^{-1})	Calculated (cm^{-1})	Assignment
–	0	Acoustic $\pm z$
–	0	Acoustic $\pm x$
–	35	O(6)$\pm x$, silicate tetrahedra rotation $\parallel z$; O(4)$-$Mg(2)$-$O(4) rotation
–	44	O(4)$-$Mg(2)$-$O(4) rotation; O(6)$\pm x$
–	67	O(4)$\pm xz$
–	85	O(1)$\pm xz$
–	95	MgO$_6$ deformation: Mg(1)$\pm x$, O(1,5)$+z$, O(6)$-z$
–	121	Mg(1)O$_6$ deformation, O(1)$\pm xz$, O(6)$\pm z$
–	164	MgO$_6$ shear along x; Mg(1)$+z$, Mg(2)$-z$, O(1)$\pm xz$
–	181	Silicate sheet compression/decompression across xz-mirror plane; O(5)$\pm zy$
231	220	Mg(1)$+xz$, O(1)$+xz$, O(5)$-xz$; O(3)$\pm xy$
–	270	Mg(1)O$_6$ rotation $\parallel y$: Mg(2)$\pm x$, O(1)$\pm xz$; O(6)$+z$, O(5)$-z$
–	298	Mg(1,2)$\pm xz$, Mg(1)$-$O(2) stretch; Si(1)$\pm xz$, O(6)$\pm xz$
313	316	Mg(1)O$_6$ deformation: Mg(1)$\pm xz$; Si(2)$-$O(3)$\pm z$
335	343	O(5)$+x$, O(6)$-x$
411	409	Mg(1)$+xz$, Mg(2)$-xz$; O(7)$+z$, O(8)$-z$
434	440	Mg(1)$+xz$, O(1)$-xz$; O(5)$\pm z$
–	467	Mg(1)$\pm z$, Mg(2)$\pm xz$; O(5,6)$+z$, O(7,8)$-z$; O(2)$-$Si(1)$-$O(8) bend
486	487	Mg(1)$\pm xz$, Si(2)$-$O(5)$\pm y$, O(8)$-$Si(2)$-$O(7) bend
–	509	Mg(2)$+z$, Mg(2)$-$O(4), O(6)$-z$
520	518	Silicate sheet deformation: O(5,6)$+x$, Si(1)$-x$, O(7)$-$Si(2)$-$O(5) bend
542	537	Mg(1)$-$O(2) stretch; Mg(1)$+x$, Mg(2)$-x$; O(5)$\pm z$
585	599	MgO$_6$ deformation: O(3)$-$Mg(1,2)$-$O(2) breathing; O(7)$\pm z$
650	646	Mg(2)$-$O(3) stretch; O(6,8)$\pm z$
650	659	Mg(1,2)$-$O(3,2) stretch, O(6)$\pm z$
737	737	Si(1,)$\pm y$, Si(1)$-$O(6)$-$Si(2) breathing, O(7)$\pm x$
799	818	Silicate sheet deformation: Si(1)$+x$, Si(2)$-x$, Si(1)$-$O(7,8)$-$Si(2) breathing
941	957	Si(2)$-$O(3), Si(2) tetrahedral base breathing; Si(1)$\pm yz$
1034	1001	Si$-$O(nb) stretch: Si(1)$-$O(2), Si(2)$-$O(3)
1092	1081	Silicate tetrahedral base breathing and Si$-$O(nb) stretch: Si(1)$-$O(2), Si(2)$-$O(3)
–	1177	Si$-$O(b) stretch: Si(2)$-$O(7,8)
1193	1192	Si$-$O(b) stretch: Si(2)$-$O(5,8), Si(1)$-$O(8)

oriented crystals) and the film (oriented with crystals in the plane of the film; B_{1u}- and B_{2u}-dominated), and selection rules allowed unambiguous vibrational species assignments to some of the peaks (Figure 6). For peaks within the low frequency envelope between 400 and 600 cm^{-1} and the prominent peaks between 950 and 1100 cm^{-1}, only a few tentative species assignments could be made (see Figure 6).

Considering that the procedure to generate the calculated modes for sepiolite was based solely on the palygorskite force constants and was independent of the features in the Raman and IR spectra, the frequency agreement between spectral features and calculated modes is reasonable (Figures 5 and 6). This is especially true when comparing the relative densities of Raman and IR modes within the various frequency ranges in the spectra (Figures 5 and 6). This result confirms that the bonding environments within the palygorskite and sepiolite structures are similar.

All sepiolite Raman and IR spectral features at frequencies >600 cm^{-1} can be described by at least one calculated mode. Below 600 cm^{-1}, the calculations predict a near continuum of modes for each vibrational species: 30 A_g, 32 B_{1g}, 30 B_{2g}, 33 B_{3g}, 31 B_{1u}, 28 B_{2u} and 31 B_{3u}, where a continuum of spectral features is observed in this frequency range in the spectra. As there are several to many calculated modes that can be assigned to each spectral feature in the data, only general Raman and IR eigenmode descriptions are presented here for sepiolite that cover specific frequency ranges in the spectra.

Eigenmode descriptions and assignments

Palygorskite. The eigenmodes calculated for palygorskite can be divided into two basic groups based on frequency ranges of the corresponding spectral features in the Raman and IR data (Figures 2 and 3). Above ~700 cm^{-1} in the IR and 750 cm^{-1} in the Raman
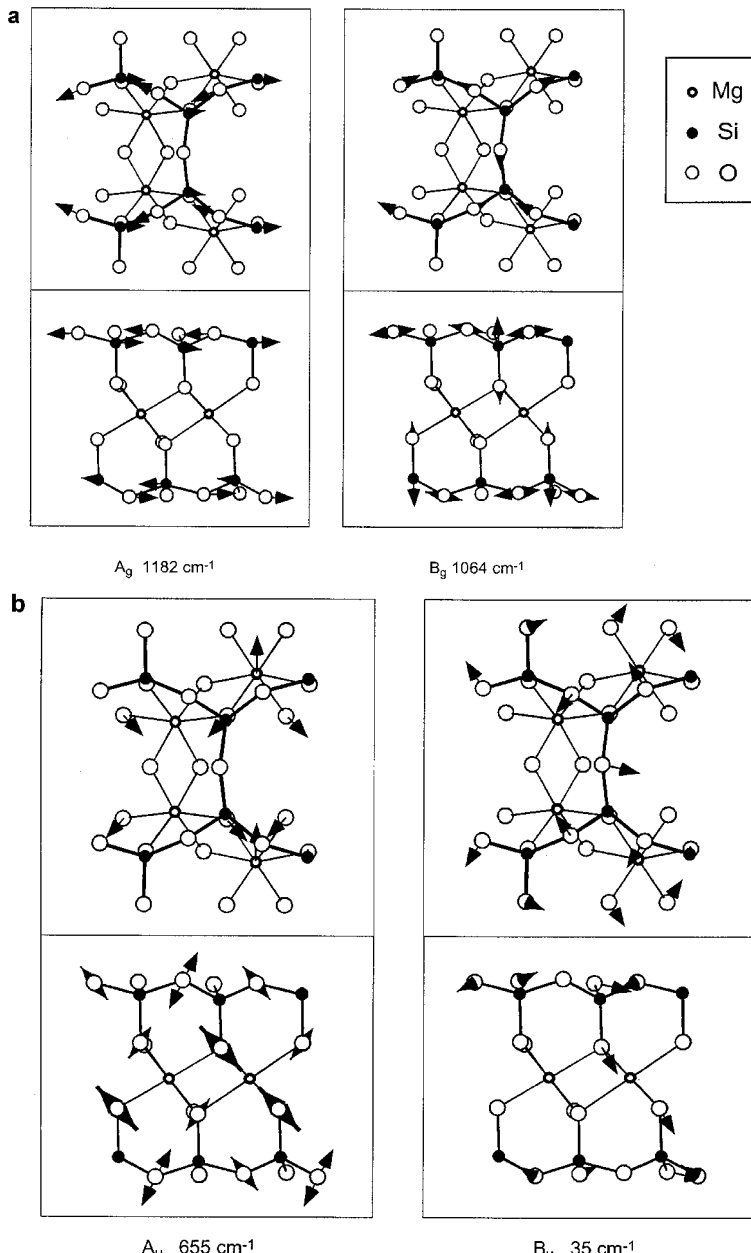
Figure 4. Eigenmode plots for palygorskite: (a) localized Si–O bond stretching (1182 cm^{-1}) and tetrahedral breathing modes within the silicate tetrahedral sheets (1064 cm^{-1}), and (b) less localized deformational modes affecting the silicate and Mg octahedral sheets (655 cm^{-1}) and silicate tetrahedral rotation (35 cm^{-1}).

spectra, the eigenmodes are dominated by atomic displacements within the silicate sheets. At the highest mode frequencies, the displacements are the most localized Si–O stretch motions, *e.g.* Si–O(nb). As mode frequencies become progressively lower, longer-range O-Si-O bend, silicate tetrahedral breathing, and shearing within the silicate sheets dominate (Tables 3–6). Below 700 cm^{-1} the eigenmodes have motions within the Mg(1)- and Mg(2)-octahedra and the silicate sheets; the eigenmodes assigned to the most prominent peaks in the Raman spectra (near 700 cm^{-1}) belong to this group.

As mode frequencies decrease, the corresponding eigenmodes evolve from more localized Mg-O-stretch, O-Mg-O-bend and O-Si-O-bend motions to longer-range motions such as silicate sheet deformations caused by silicate tetrahedra rotation and silicate sheet shearing around the Mg octahedral sheets deforming the Mg octahedra. The eigenmode *vs.* frequency trends outlined above are also followed by muscovite and phlogopite (McKeown *et al.*, 1999a,b), including the internal silicate sheet displacements above 700 cm^{-1}, and octahedral and silicate sheet displacement mixtures

Table 7a. Irreducible representations for the sepiolite structure, excluding zeolitic water.

Atom Types	Site symm.	$A_g(R)$	$B_{1g}(R)$	$B_{2g}(R)$	$B_{3g}(R)$	A_u	$B_{1u}(IR)$	$B_{2u}(IR)$	$B_{3u}(IR)$
Mg(1),Mg(2), Mg(3),Mg(4)	2	1	2	1	2	1	2	1	2
O(3)	2	1	1	2	2	1	1	2	2
Si(1),Si(2),Si(3), O(1a),O(1b),O(1c), O(2a),O(2b),O(2c), O(2d),OH,H₂O(1)	1	3	3	3	3	3	3	3	3
N_{total}		41	45	42	46	41	45	42	46

Note: conventions in Table 1 apply. B_{1u}, B_{2u} and B_{3u} species include 1 acoustic mode each.

Table 7b. Force constant values used for sepiolite.

Interaction	Value
Si−O(b) Si−O(nb)	4.85×10^5 dyne/cm 4.82
Mg(1,2,3)−O Mg−OH	0.94
Mg(4)−O Mg(4)−H₂O	1.37
O(nb)−Si−O(b)	1.20×10^{-11} erg
O(b)−Si−O(b)	1.10
Mg−O−Si	0.22
O−Mg−O O−Mg−OH OH−Mg−OH O−Mg−H₂O H₂O−Mg−H₂O	0.08

Note: O(b) includes O(2a), O(2b), O(2c), O(2d) and O(3); O(nb) includes O(1a), O(1b) and O(1c). Atom notations are those of Brauner and Preisinger (1956). The force constants are taken from equivalent values derived from the palygorskite calculation.

below 700 cm⁻¹. The palygorskite structure has O(4) atoms that terminate the Mg(2) octahedra and are not bonded to another cation. Fundamental modes with mostly Mg(2)-O(4)-stretch and O(4)-Mg(2)-O(4)-bend-rotation displacements dominate the lowest frequency modes (Tables 3−6), that are generally not recorded in either the Raman or IR spectra.

Sepiolite. Considering the force constants used in this calculation, it is not surprising that the eigenmode *vs.* frequency trends follow those outlined above for palygorskite. Due to the simplified nature of calculation performed for sepiolite, the Raman and IR eigenmode assignments are outlined in some detail with the spectra (Figures 5 and 6) rather than having all 345 optic modes listed exhaustively in eight tables. Similar to palygorskite, the localized internal silicate sheet modes are generally above 700 cm⁻¹ and the less localized Mg octahedra and silicate sheet displacement mixtures

(labeled 'Deformations' in Figures 5 and 6) are below 700 cm⁻¹. The deformations for sepiolite also include modes dominated by OH and H₂O motions within the Mg octahedra. As in palygorskite, the sepiolite structure has water molecules coordinated to the octahedra at the edges of the ribbons [Mg(4)] and the fundamental modes dominated by Mg(4)-H₂O stretch and H₂O-Mg(4)-H₂O bend-rotation displacements are at the lowest frequencies, which are also not recorded in either the Raman or IR spectra.

Comparisons with earlier IR and Raman studies

A number of papers present IR and Raman data with some vibrational assignments for sepiolite and palygorskite in the context of acid treatments of these phases or adsorption of organic molecules by these phases (Akyuz *et al.*, 1993; Akyuz *et al.*, 1995; Belzunce *et al.*, 1998; Mendelovici, 1973; Myriam *et al.*, 1998; Vicente-Rodriguez *et al.*, 1996). In general, the IR spectra in these studies are similar to those plotted in Figures 3 and 6. The unpolarized Raman spectrum of sepiolite in Akyuz *et al.* (1995) is also similar (minus the pyrazine modes) to our polarized spectra in Figure 5. Most vibrational assignments made in these studies are for water and hydroxide modes above 1500 cm⁻¹, and beyond the scope of this work. However, some assignments are made to lower frequency IR features for both palygorskite and sepiolite that are generally consistent with our findings from the calculations. Mendelovici (1973) studied HCl- as well as D₂O-treated attapulgite (palygorskite) by using IR spectra to detect changes in bands assigned to Si-O, Si-O-Si and OH vibrations. Generally, the assignments for some of the lower-frequency modes presented for palygorskite, such as the 1198 cm⁻¹ mode assigned to Si-O vibrations, are in agreement with the lattice dynamics results (Figure 3). The dissolution of the octahedral sheets in HCl-treated palygorskite causes changes to the 985, 1030 and 1198 cm⁻¹ Si-O vibration bands, where the silicate sheets presumably convert to silanol groups. These interpretations are again consistent with the vibrational assignments for palygorskite in Figure 3, where Si-O
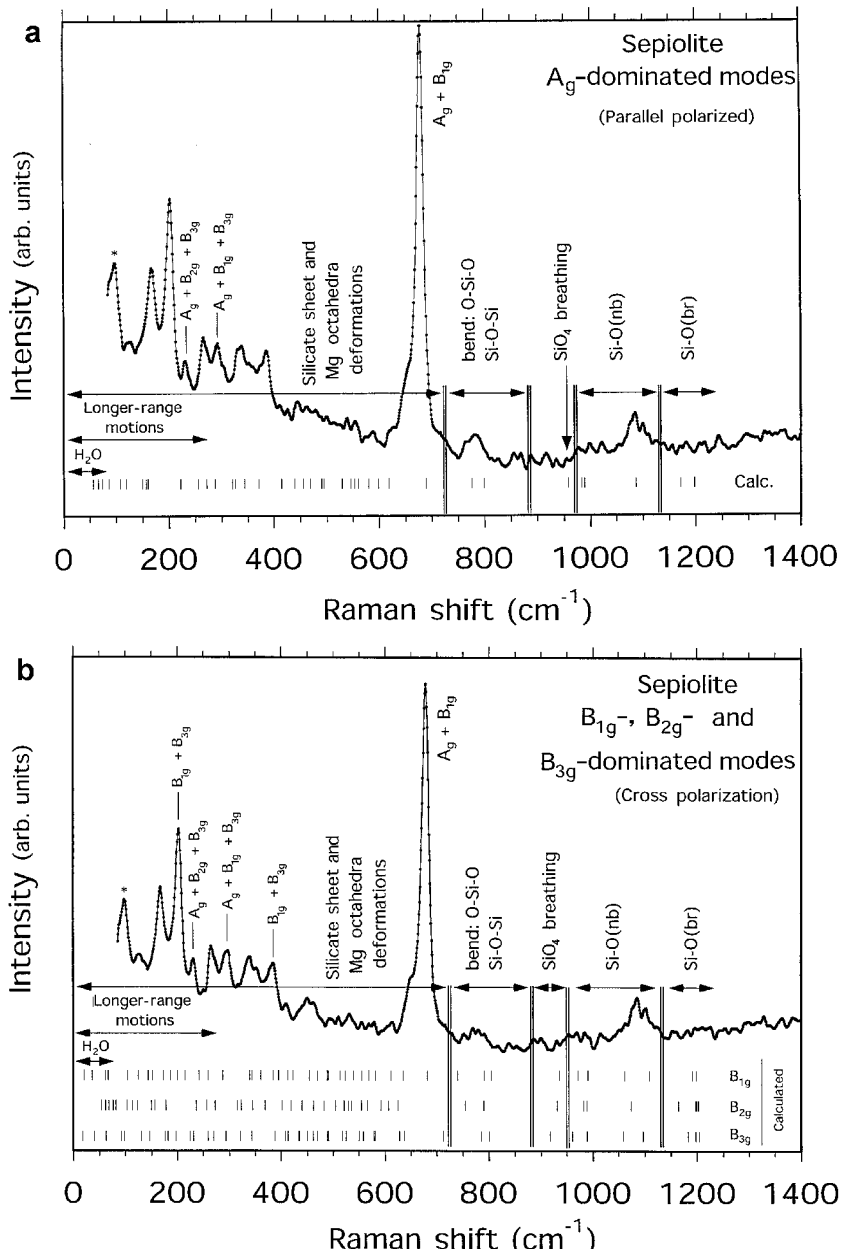
Figure 5. Raman spectra of sepiolite (a) parallel polarized Raman spectrum with some general vibrational assignments from the calculations and plausible vibrational species assignments to some peaks. Calculated mode frequencies are indicated from the model that used final force constants determined for palygorskite as applied to the sepiolite structure. Silicate sheet and Mg octahedral deformations indicate vibrational modes involving motions of three or more atom types within the silicate tetrahedral and Mg octahedral sheets that include Mg-OH and Mg-H$_2$O stretching as well as OH-Mg-OH and H$_2$O-Mg-H$_2$O bending modes. Longer-range motions indicate vibrational modes involving longer-range translational, rotational and shear displacements of the silicate tetrahedral and Mg octahedral sheets. * indicates an artifact from the laser line filter cut-off. (b) Cross-polarized Raman spectrum of sepiolite with some general vibrational assignments from the calculations. Conventions in (a) apply.

displacements are assigned to all modes at frequencies greater than 970 cm^{-1} (shown in Mendelovici, 1973), while any octahedral sheet modes are below 700 cm^{-1} (not shown in Mendelovici, 1973). One discrepancy in the literature is found for the assignment to the 648 cm^{-1} IR mode for sepiolite: Belzunce *et al.* (1998)

assigned this mode to OH-Mg-OH bend, where calculated IR modes near 650 cm^{-1} for sepiolite are dominated by H$_2$O-Mg-H$_2$O bend, Mg octahedra deformations and silicate sheet deformations.

Most of these papers note differences in the IR spectra below 1500 cm^{-1} that may be attributed to the
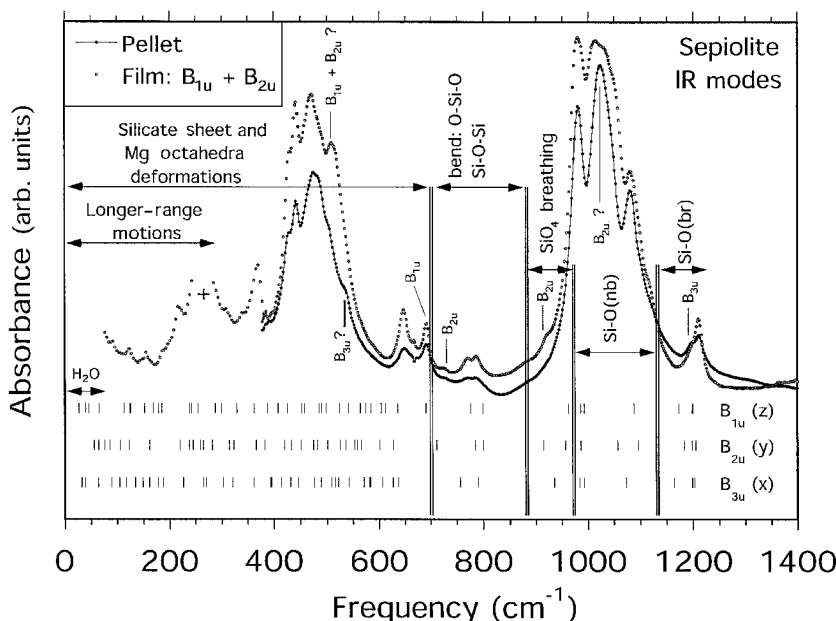
Figure 6. IR spectra of sepiolite with general vibrational assignments from the calculations. Because of the fibrous crystal morphology of sepiolite, the spectrum of the thin film is dominated by B_{1u} and B_{2u} modes, while the spectrum of the pellet has a more random mixture of all IR-active modes. Conventions in Figure 5 apply. + indicates the far IR frequency range for the film that was not plotted due to an artifact arising from the mylar beamsplitter.

decomposition or alteration of Mg or Al octahedral sheets in the parent phase. Many of these differences are not large and can be described as relative intensity changes of IR bands; these spectral differences are similar to changes seen between the IR spectra of the pellet and film samples for sepiolite and palygorskite (Figures 3 and 6). With this in mind, changes in the low frequency IR features of treated sepiolite or palygorskite samples, may be from textural changes for the fibers (as shown in Belzunce *et al.*, 1998), rather than from alteration of the octahedral sheet in the crystal structure. Various stages of these treatments can change the fiber morphology in different ways, and therefore, can change the way in which the fibers randomly or pseudo-randomly orient themselves within an IR sample. These orientation differences in the fibers can change the relative dominance of the vibrational species, and as a result, change the relative intensities of families of bands in the IR spectrum for that material.

Similar to conclusions made for phlogopite and muscovite (McKeown *et al.*, 1999a,b), specific eigen-mode assignments made to Raman and IR modes in this study do not agree particularly well with assignments made in a study of optical vibrations in sheet silicates by Loh (1973). The discrepancies are probably due to the fact that Loh made vibrational assignments based on the MO_6 octahedral and TO_4 tetrahedral symmetry of atom clusters in phyllosilicates and observations of Raman modes from similar atom clusters in other materials; whereas the eigenmodes calculated here are based on the palygorskite and sepiolite structures. Loh's general

arguments agree to some extent with our findings, but many discrepancies are seen in the details. According to Loh, Raman modes at frequencies >300 cm^{-1} are dominated by T-O-stretch motions within the tetrahedra. This argument is partially supported by our findings for palygorskite and sepiolite, but Raman active eigenmodes up to 700 cm^{-1} can be dominated by Mg octahedral motions. According to Loh, MO_6 octahedral modes dominate at frequencies <200 cm^{-1}. We find that most eigenmodes in this frequency range do contain Mg octahedral motions that can be mixed with silicate tetrahedral sheet rotations and deformations. Some modes, such as the calculated 181 cm^{-1} B_u mode for palygorskite, is dominated by displacements within the silicate sheets.

CONCLUSIONS

The work described here is the first comprehensive attempt to use lattice dynamic calculations to interpret features in palygorskite and sepiolite IR and Raman spectra. Calculations show that vibrational modes above ~700 cm^{-1} in IR and 750 cm^{-1} in Raman spectra are dominated by atomic displacements within the silicate sheets, and below these values by motions among the octahedral and silicate sheets. The Si–O stretch and O–Si–O-bond bending force constants for palygorskite are similar to values reported previously for other silicates. The Mg–O-bond stretch force constants, on the other hand, are about half of the comparable values determined for the octahedral sheets in micas. The

weaker octahedral bonding environments in palygorskite and sepiolite allow for increased cation substitution relative to micas.

REFERENCES

Ahlrichs, J.L., Serna, C. and Serratosa, J.M. (1975) Structural hydroxyls in sepiolites. *Clays and Clay Minerals*, **23**, 119–124.

Akyuz, S., Akyuz, T. and Davies, J.E.D. (1993) An FT-IR spectroscopic investigation of the adsorption of benzidine by sepiolite from Eskisehir (Turkey). *Journal of Molecular Structure*, **293**, 279–282.

Akyuz, S., Akyuz, T., Davies, J.E.D., Esmer, K. and Erbolukbas Ozel, A. (1995) Fourier transform Raman and Fourier transform IR spectroscopic investigation of pyrazine adsorbed by sepiolite and bentonite from Anatolia. *Journal of Raman Spectroscopy*, **26**, 883–888.

Belzunce, M.J., Mendioroz, S. and Haber, J. (1998) Modification of sepiolite by treatment with fluorides: structural and textural changes. *Clays and Clay Minerals*, **46**, 603–614.

Blanco, C., Herrero, J., Mendioroz, S. and Pajares, J.A. (1988) Infrared studies of surface acidity and reversible folding in palygorskite. *Clays and Clay Minerals*, **36**, 364–368.

Bradley, W.F. (1940) The structural scheme of attapulgite. *American Mineralogist*, **25**, 405–410.

Brauner, K. and Preisinger, A. (1956) Struktur und Entstehung des Sepioliths. *Tschermaks Mineralogische und Petrographische Mitteilungen*, **6**, 120–140.

Chisholm, J.E. (1992) Powder diffraction patterns and structural models for palygorskite. *The Canadian Mineralogist*, **30**, 61–73.

Christ, C.L., Hathaway, J.C., Hostetler, P.B. and Shepard, A.O. (1969) Palygorskite: new X-ray data. *American Mineralogist*, **54**, 198–205.

Dowty, E. (1987) Fully automated microcomputer calculation of vibrational spectra. *Physics and Chemistry of Minerals*, **14**, 67–79.

Drits, V.A. and Sokolova, G.V. (1971) Structure of palygorskite. *Soviet Physics and Crystallography*, **16**, 183–185.

Fateley, W.G., Dollish, F.R., McDevitt, N.T. and Bentley, F.F. (1972) *Infrared and Raman Selection Rules for Molecular and Lattice Vibrations: the Correlation Method*. Wiley, New York.

Frost, R.L., Cash, G.A. and Kloprogge, J.T. (1998) 'Rocky Mountain leather', sepiolite and attapulgite – an infrared emission spectroscopic study. *Vibrational Spectroscopy*, **16**, 173–184.

Galán, E. and Carretero, M.I. (1999) A new approach to compositional limits for sepiolite and palygorskite. *Clays and Clay Minerals*, **47**, 399–409.

Hayashi, H. (1969) Infrared study of sepiolite and palygorskite on heating. *American Mineralogist*, **53**, 1613–1624.

Jones, B.F. and Galán, E. (1988) Sepiolite and palygorskite. Pp. 631–674 in: *Hydrous Phyllosilicates* (S.W. Bailey, editor). Reviews in Mineralogy, **19**, Mineralogical Society of America, Washington, D.C.

Kim, C.C., Bell, M.I. and McKeown, D.A. (1993) Vibrational analysis of benitoite and the Si_3O_9 ring. *Physical Review*, **B 47**, 7869–7877.

Loh, E. (1973) Optical vibrations in sheet silicates. *Journal of Physics, C: Solid State Physics*, **6**, 1091–1104.

Loudon, R. (1964) Raman scattering from crystals. *Advances in Physics*, **13**, 423–482.

McKeown, D.A., Bell, M.I. and Etz, E.S. (1999a) Raman spectra and vibrational analysis of the trioctahedral mica phlogopite. *American Mineralogist*, **84**, 970–976.

McKeown, D.A., Bell, M.I. and Etz, E.S (1999b) Vibrational analysis of the dioctahedral mica: $2M_1$ muscovite: . *American Mineralogist*, **84**, 1041–1048.

Mendelovici, E. (1973) Infrared study of attapulgite and HCL treated attapulgite. *Clays and Clay Minerals*, **21**, 115–119.

Mendelovici, E. and Portillo, D.C. (1976) Organic derivatives of attapulgite – I. Infrared spectroscopy and X-ray diffraction studies. *Clays and Clay Minerals*, **24**, 177–182.

Myriam, M., Suarez, M. and Martin-Pozas, J.M. (1998) Structural and textural modifications of palygorskite and sepiolite under acid treatment. *Clays and Clay Minerals*, **46**, 225–231.

Preisinger, A. (1963) Sepiolite and related compounds: its stability and application. *Clays and Clay Minerals*, **10**, 365–371.

Ruiz-Hitzky, E. (2001) Molecular access to intracrystalline tunnels of sepiolite. *Journal of Materials Chemistry*, **11**, 86–91.

Serna, C., VanScoyoc, G.E. and Ahlrichs, J.L. (1977) Hydroxyl groups and water in palygorskite. *American Mineralogist*, **62**, 784–792.

VanScoyoc, G.E., Serna, C.J. and Ahlrichs, J.L. (1979) Structural changes in palygorskite during dehydration and dehydroxylation. *American Mineralogist*, **64**, 215–223.

Vicente-Rodriguez, M.A., Suarez, M., Bañares-Munoz, M.A. and de Dios Lopez-Gonzalez, J. (1996) Comparative FT-IR study of the removal of octahedral cations and structural modifications during acid treatment of several silicates. *Spectrochimica Acta*, **A52**, 1685–1694.

Wang, Q.K., Matsuura, T., Feng, C.Y., Weir, M.R., Detellier, C., Rutadinka, R.L. and Van Mao, R.L. (2001) The sepiolite membrane for ultrafiltration. *Journal of Membrane Science*, **184**, 153–163.